Ultrafine dual-phased carbide nanocrystals confined in porous nitrogen-doped carbon dodecahedrons for efficient hydrogen evolution reaction

Lu, Xue Feng; Yu, Le; Zhang, Jintao; Lou, David Xiong Wen

2019

Lu, X. F., Yu, L., Zhang, J., & Lou, D. X. W. (2019). Ultrafine dual-phased carbide nanocrystals confined in porous nitrogen-doped carbon dodecahedrons for efficient hydrogen evolution reaction. Advanced Materials, 31(30), 1900699-. doi:10.1002/adma.201900699

https://hdl.handle.net/10356/138565

https://doi.org/10.1002/adma.201900699

Ultrafine Dual-phased Carbide Nanocrystals Confined in Porous Nitrogen-doped Carbon Dodecahedrons for Efficient Hydrogen Evolution Reaction

*Xue Feng Lu, Le Yu, Jintao Zhang, and Xiong Wen (David) Lou**

[*] Dr. X. F. Lu, Dr. L. Yu, Dr. J. T. Zhang, Prof. X. W. Lou

School of Chemical and Biomedical Engineering, Nanyang Technological University, 62 Nanyang Drive, Singapore 637459, Singapore
Email: xwlou@ntu.edu.sg; davidlou88@gmail.com
Webpage: http://www.ntu.edu.sg/home/xwlou/

Abstract

Designing novel nonnoble electrocatalysts with controlled structures and composition remains a great challenge for efficient hydrogen evolution reaction (HER). Herein, we report a rational synthesis of ultrafine carbide nanocrystals confined in porous nitrogen-doped carbon dodecahedrons (PNCDs) by annealing functional zeolitic imidazolate framework (ZIF-8) with molybdate or tungstate. By controlling the substitution amount of MO_4 units (M = Mo or W) in the ZIF-8 framework, dual-phase carbide nanocrystals confined in PNCDs (denoted as MC-M_2C/PNCDs) can be obtained, which exhibit superior activity toward HER to the single-phased MC/PNCDs and M_2C/PNCDs. The evenly distributed ultrafine nanocrystals favor the exposure of active sites. Porous nitrogen-doped carbon dodecahedrons as the support facilitate the charge transfer and protect the nanocrystals from aggregation during the HER process. Moreover, the strong coupling interactions between MC and M_2C provide beneficial sites for both water dissociation and hydrogen desorption. This work highlights a new feasible strategy to explore efficient electrocatalysts via engineering on nanostructure and composition.

Keywords: dual-phased; carbides; N-doped carbon; electrocatalysis; hydrogen evolution reaction

Water electrolysis for hydrogen is the main component of clean-energy technologies,[1,2] such as proton exchange membrane electrolyzers, water-alkali electrolyzers, and chlor-alkali electrolyzers. However, due to the strongly uphill with large overpotential during the hydrogen evolution reaction (HER), the practical applications of water electrolysis are very limited.[3] Towards that end, one key challenge lies in the development of low-cost but efficient electrocatalysts to accelerate the electrochemical process of HER.[4] Interest in the low-cost transition metal carbides has been aroused by their Pt-like d-band density of states,[5,6] tunable phase and composition related to varied electronic features,[7,8] good physical and chemical stability,[9] as well as high conductivity.[10,11]

As two of the most efficient carbides for HER, molybdenum/tungsten carbides with different morphologies and compositions have been extensively investigated. Many approaches, including chemical vapor deposition (CVD),[12,13] pyrolysis of metal complexes,[14,15] and carburization of the mixed Mo/W-based compounds and carbon sources, have been developed.[16,17] However, these traditional methods usually suffer from the inevitable aggregation and/or uncontrollable particle sintering with excessive growth at high temperatures, which may lead to the loss of active sites.[6,16,18] To further improve the electrocatalytic performance, three main strategies have been developed as follows: (i) nano-structuring to provide larger specific surface areas and expose more active sites;[8,14] (ii) doping of heteroatoms to modify the electronic state of the metal elements;[12,19] (iii) compositing with carbon-based materials to improve the conductivity and stability of carbides.[20-22] Nevertheless, construction of ultrafine dual-phase carbides within nitrogen-rich carbon matrix has rarely been reported until now.[8,23]

Recently, metal-organic frameworks (MOFs) have been regarded as the ideal reactive precursors to establish well-defined nanocrystals due to their highly ordered porous structures and diversified

metal nodes/organic ligands.[24-26] In this work, Zn-based zeolitic imidazolate framework (ZIF-8) substituted with MO_4 units (denoted as ZIF-8-MO_4) dodecahedrons are obtained through an anion exchange reaction between the Zn(imidazolate)$_4^{2-}$ units in ZIF-8 and MO_4^{2-} anions in inorganic salts. Their similar four-connected open frameworks ensure the reaction possible.[27] Benefiting from the internal long-range ordered Zn-O-M connectivity, high carbon/nitrogen content, low boiling point of Zn, and high porosity of ZIF-8, the in-situ generated carbides are evenly dispersed within the PNCDs in the form of ultrafine nanocrystals. The ultrafine nanocrystals confined within this porous nanostructure results in the strong contact between the carbides and the conductive carbon support, which not only provides more stable active sites but also facilitates the electron transport in the HER process.[18,21,28] Besides, the abundant nitrogen dopants can function as electron acceptors to assist the carbon atoms in the metal lattice, which is immensely conducive to enhance the catalytic activity.[16] Benefiting from the advantages of ultrafine nanocrystals and porous nitrogen-doped carbon support, the as-prepared carbides show high electrocatalytic activity and stability. Moreover, the dual-phase MC-M_2C nanocrystals can be obtained by a moderate substituted amount of MO_4 units in the framework of ZIF-8. The strong coupling interactions between MC and M_2C nanocrystals further provide beneficial sites for both water dissociation and hydrogen desorption,[8,11] resulting in much higher catalytic activity than that of single-phased MC and M_2C.

The synthesis strategy of the MC-M_2C/PNCDs composite is illustrated in **Figure 1**. Uniform ZIF-8 dodecahedrons are first obtained according to the modified method reported elsewhere.[29] The field-emission scanning electron microscope (FESEM) and transmission electron microscope (TEM) images (**Figure 2**a) show the uniformly solid ZIF-8 dodecahedrons with an average diameter of 515 nm (Figure S1a,b, Supporting Information). Subsequently, ZIF-8-MO_4-100 (100 stands for the

quantity of molybdate/tungstate) dodecahedrons are prepared through an anion exchange reaction. The FESEM and TEM images (Figure 2b,c) show the intact morphology and structure except for the smooth corner and slightly smaller size (Figure S1c-f, Supporting Information), which may be due to the partial dissolution/recrystallization and shorter nodal distance between Zn-O-M than that of Zn-imidazolate-Zn.[27] X-ray diffraction (XRD) patterns (Figure 2d) demonstrate that ZIF-8 is the only crystalline phase without obvious damage in crystallinity.[29] A new peak at ~843.5 cm^{-1} in the Fourier-transform infrared (FTIR) spectra (Figure 2e) shows that MO_4 units are successfully substituted in the framework of ZIF-8.[17] Energy-dispersive X-ray (EDX) spectra also clearly show the existence of Mo or W and O (Figure S2, Supporting Information). The absence of sodium element rules out the possibility of inclusion of molybdate or tungstate in the framework by adsorption. Notably, the nitrogen sorption isotherms of ZIF-8 and ZIF-8-MO_4-100 are almost identical (Figure S3, Supporting Information), indicating the intactness of the ordered structure of ZIF-8 after inclusion of MO_4. The Brunauer-Emmett-Teller (BET) surface area of the as-prepared ZIF-8, ZIF-8-MoO_4-100, and ZIF-8-WO_4-100 is calculated to be 1532, 1161 and 1140 $m^2\ g^{-1}$, respectively, which is consistent with the value of ZIF-8 reported elsewhere.[29,30] The same pore size distribution (Figure 2f) also implies the pores of ZIF-8 are not blocked by the MO_4 units. All these results strongly suggest that MO_4 units are substituted in the ZIF-8 framework but not through the adsorption or encapsulation.

During the pyrolysis, the organic ligands can be converted into carbon, which can react with adjacent Mo or W atoms to form ultrafine carbide nanocrystals while generating CO_2 gas. The releasing of gas and the evaporation of zinc generate the porous structure. As expected, the derived MC-M_2C/PNCDs maintain uniform morphology with ultrafine nanocrystals confined in porous carbon dodecahedrons, and the average size is approximately 390 nm for MoC-Mo_2C/PNCDs

(**Figure 3**a,b) and 420 nm for WC-W_2C/PNCDs (Figure 3e,f). The high-resolution TEM (HRTEM) images show the presence of ultrafine nanocrystals with ~ 5 nm in size for both MoC-Mo_2C and WC-W_2C (Figure 3c,g). The clear lattice fringes in Figure 3c with an inter-planar spacing of 0.25 nm and 0.22 nm are assigned to the (100) planes of MoC and (101) planes of Mo_2C (Figure S4, Supporting Information). The clear lattice fringes in Figure 3g with an inter-planar spacing of 0.25 nm and 0.23 nm can be readily assigned to the (100) planes of WC and (102) planes of W_2C (Figure S5, Supporting Information). Elemental mapping images (Figure 3d,h) show the homogenous distribution of C, N, Mo or W elements in the MC-M_2C/PNCDs.

XRD analysis (**Figure 4**a,b) indicates that the primary crystalline phases are MoC (JCPDS No. 06-0546) and Mo_2C (JCPDS No. 35-0787) in the derivative from ZIF-8-MoO_4-100, while WC (JCPDS No. 51-0939) and W_2C (JCPDS No. 20-1315) in the derivative from ZIF-8-WO_4-100. More information about carbon species in the resultant hybrids is provided by the Raman spectra (Figure 4c). As a comparison, PNCDs derived from ZIF-8 are obtained (Figure S6, Supporting Information). The higher intensity ratio of peak G to peak D indicates that more sp^2-hybridized carbon atoms are present in the MC-M_2C/PNCDs, which may be beneficial for accelerating the charge transfer rate and stabilizing the carbide nanocrystals.[9,31] The EDX (Figure 4d) results also confirm the existence of only C, N, Mo or W elements in MC-M_2C/PNCDs, which is consistent with the results of elemental mapping. Combining the difference in mass before and after dissolving carbides and the total molar number of metal, the molar ratio of MC/M_2C in MC-M_2C/PNCDs can be estimated to be around 0.75 for MoC-Mo_2C/PNCDs and 0.43 for WC-W_2C/PNCDs. Nitrogen sorption curves reveal that all the derivatives possess obvious mesoporous feature, as illustrated by typical type IV isotherms with a specific surface area of 751 $m^2 g^{-1}$ for PNCDs, 202 $m^2 g^{-1}$ for MoC-Mo_2C/PNCDs, and 153 $m^2 g^{-1}$

for WC-W_2C/PNCDs (Figure S7, Supporting Information). X-ray photoelectron spectroscopy (XPS) study was carried out to further analyze the surface chemical states of MC-M_2C/PNCDs. The existence of only C, N, Mo or W elements shows the purity of as-prepared MC-M_2C/PNCDs (Figure S8a,d, Supporting Information). In the high-resolution XPS spectra of the Mo 3d (Figure 4e) and W 4f (Figure 4f) region, there are both two pairs of peaks. The first pair of peaks at lower binding energy (228.90 eV for Mo $3d_{5/2}$ and 231.94 eV for Mo $3d_{3/2}$) is assigned to Mo-Mo or Mo-C bands. The second pair of peaks at higher binding energy (232.93 eV for Mo $3d_{5/2}$ and 236.09 eV for Mo $3d_{3/2}$) is assigned to Mo-O bands due to the slight surface oxidation of carbides.[8,11,23] Similarly, the first pair of peaks at lower binding energy (32.05 eV for W $4f_{7/2}$ and 34.14 eV for W $4f_{5/2}$) is assigned to W-W or W-C bands, and the second pair of peaks at higher binding energy (35.42 eV for W $4f_{7/2}$ and 37.57 eV for W $4f_{5/2}$) is assigned to W-O bands, specially the peak at 41.41 eV is assigned to the loss feature of W 4f.[11,18,23] The XPS spectra of C1s (Figure S8b,e, Supporting Information) can be deconvoluted into metal-C bands from carbides, C-C/C=C or C-N bands from PNCDs and C-O bands from the surface oxidized carbon or adsorbed oxygen-containing species.[17,32] The high-resolution N 1s peaks (Figure S8c,f, Supporting Information) can be deconvoluted into three peaks, indexed to pyridinic-N, pyrrolic-N and graphitic-N, which reveals the electronic status of dopants in carbon.[15,16]

Interestingly, the samples consisting of single-phased MC or M_2C can be obtained by only adjusting the amount of molybdate or tungstate in the reaction. A similar phenomenon can also be observed in synthesis of other carbides.[33,34] Solid ZIF-8-MO_4-50 and ZIF-8-MO_4-150 dodecahedrons are obtained with an amount of 50 and 150 mg of molybdate/tungstate added in the reaction. They are highly uniform with an average diameter of 490 nm for ZIF-8-MoO_4-50, 447 nm for ZIF-8-MoO_4-150, 487 nm for ZIF-8-WO_4-50 and 472 nm for ZIF-8-WO_4-150 (Figure S9,10,

Supporting Information). After annealing, MoC/PNCDs, Mo_2C/PNCDs, WC/PNCDs and W_2C/PNCDs are obtained with the similar morphology and structure (**Figure 5**a-d) to those of dual-phased MC-M_2C/PNCDs. XRD patterns (Figure 5e,f) show the single crystal phase of MC or M_2C in the corresponding derivatives. Raman spectra (Figure S11, Supporting Information) show the poorer degree of graphitization in MC/PNCDs and better degree in M_2C/PNCDs than that in MC-M_2C/PNCDs. Nitrogen sorption curves (Figure S12, Supporting Information) reveal that the derived single-phased carbides also possess obvious mesoporous feature with a specific surface area of 218 $m^2 g^{-1}$ for MoC/PNCDs, 71 $m^2 g^{-1}$ for Mo_2C/PNCDs, 125 $m^2 g^{-1}$ for WC/PNCDs and 84 $m^2 g^{-1}$ for W_2C/PNCDs. The reduction in specific surface area may be due to the consumption of carbon materials and the increase in carbide content.

The electrocatalytic performance toward HER of these M_xC/PNCDs nanocomposites is evaluated in an alkaline solution (1.0 M KOH) by a standard three-electrode system. **Figure 6**a shows the linear sweep voltammetry (LSV) curves with *iR*-compensation of MoC/PNCDs, MoC-Mo_2C/PNCDs and Mo_2C/PNCDs. It can be observed that Mo_2C/PNCDs afford smaller overpotential and higher current density toward HER than that of MoC/PNCDs, which is due to its electron configuration around the Fermi level that benefits the reduction of hydrogen.[5,7] However, the negative hydrogen-binding energy (ΔG_H*) on Mo_2C indicates a strong adsorption of H on the Mo_2C surface, which benefits H^+ reduction (i.e., Volmer step), but restricts H_{ads} desorption (i.e., the Heyrovsky/Tafel step),[5,35,36] which impedes the further improvement of HER. It is notable that the electron density around the Mo active sites mostly relies on the carbon atoms in the lattice, which will be reduced with increasing carbon because of the electron transfer from Mo to C.[8,37,38] For example, with a high C content, MoC usually shows weaker hydrogen binding than Mo_2C, and

consequently a facilitated Heyrovsky/Tafel step, but a hindered Volmer reaction.[7,39] As such, regarding the respectively promoted elementary reactions of HER on Mo_2C and MoC, when the two single-phased carbides coexist in the PNCDs, the synergistic effect on MoC-Mo_2C interfaces further promotes the HER process, resulting in the smaller onset potential (Figure S13a, Supporting Information) and overpotential than that of Mo_2C/PNCDs at the same current density (Figure 6b). To reach a current density of 10 mA cm^{-2}, which is a common criterion to evaluate HER activity, the dual-phased MoC-Mo_2C/PNCDs need an overpotential of only 121 mV. On the other hand, 49 and 28 mV higher overpotentials are required for MoC/PNCDs and Mo_2C/PNCDs respectively, to achieve the same current density. Moreover, the rise of the current densities of the dual-phased MoC-Mo_2C/PNCDs is much faster than those of single-phased MoC/PNCDs and Mo_2C/PNCDs. Specifically, the current density of the dual-phased MoC-Mo_2C/PNCDs could increase to 100 mA cm^{-2} at the overpotential of 182 mV, which is 87 and 49 mV lower than those of MoC/PNCDs and Mo_2C/PNCDs, respectively. The rapid rise in current density can also be reflected by the dynamic process using Tafel slopes (Figure 6c). The smallest Tafel slope of MoC-Mo_2C/PNCDs (60 mV dec^{-1}) implies the favorable hydrogen evolution. The exchange current density is determined to be 0.15 mA cm^{-2} by fitting the linear portion of the Tafel plot at low current density (Figure S13b, Supporting Information). The highest value also indicates the best intrinsic electrocatalytic activity of MoC-Mo_2C/PNCDs.[23,40,41] The smallest charge transfer resistance (R_{ct}) during the HER process (Figure S14, Supporting Information) also suggests the most efficient HER kinetics.[42,43] The fitting data of R_{ct} for Mo_xC/PNCDs are listed in Table S1. Furthermore, the MoC-Mo_2C/PNCDs exhibit the highest electric double layer capacitance of 0.47 F cm^{-2} (Figure S15, Supporting Information), implying the highest electrochemically active surface area (ECSA).[16,44] The higher ECSA indicates that more

effective active sites can be exposed in MoC-Mo_2C/PNCDs, in line with the more excellent HER performance. The specific comparison of the electrocatalytic performances for Mo_xC/PNCDs is listed in Table S3.

To compare the electrocatalytic performances of the Mo_xC/PNCDs with those of the recently reported molybdenum-carbide-based HER electrocatalysts and commercial 20 wt% Pt/C (Figure S16a,b, Supporting Information) electrocatalysts, the overpotential required to drive 10 mA cm^{-2} (η_{10}) and the Tafel slope are summarized in Figure 6d (also see Table S3, Supporting Information), showing a competitive performance. It is noted that the MoC-Mo_2C/PNCDs only need a small overpotential without an obvious increase to drive a current density of 10 mA cm^{-2} for 20 h (Figure S17a,b, Supporting Information), which is much better than that of commercial 20 wt% Pt/C electrocatalysts (Figure S16c, Supporting Information), implying the excellent stability. FESEM and TEM images after the stability test (Figure S17c, Supporting Information) also confirm the superior durability of the structure.

Tungsten-based materials, especially WC and W_2C, are also considered attractive candidates to replace the costly Pt-based electrocatalysts for HER.[6,21] Herein, we also compare the HER performance of the as-prepared WC/PNCDs, WC-W_2C/PNCDs and W_2C/PNCDs. Similar to the trend observed for aforementioned Mo_xC/PNCDs, the dual-phased WC-W_2C/PNCDs show the best HER performance with an overpotential of 101 and 192 mV to achieve a current density of 10 and 100 mA cm^{-2}, respectively (Figure 6e,f). The onset potential is only 11 mV (Figure S18a, Supporting Information), which is not only the smallest value among the W_xC/PNCDs but also smaller than that of MoC-Mo_2C/PNCDs (45 mV). Tafel plots also show the kinetic advantage toward HER of WC-W_2C/PNCDs with the smallest value of 90 mV dec^{-1} (Figure 6g) and highest exchange current density

of 0.74 mA cm^{-2} (Figure S18b, Supporting Information). The results of ECSA and electrochemical impedance spectroscopy (EIS) indicate the dual-phased WC-W_2C/PNCDs possess more active sites and faster charge-transfer ability (Figure S19,20, Supporting Information). The specific comparison of the electrocatalytic performance among the as-prepared W_xC/PNCDs is listed in Table S4. In view of η_{10} and Tafel slope, the dual-phased WC-W_2C/PNCDs also show a strong competition compared to other reported tungsten-carbide-based electrocatalysts and commercial 20 wt% Pt/C electrocatalysts (Figure 6h, Figure S16, Table S5, Supporting Information). Moreover, the as-prepared WC-W_2C/PNCDs show excellent stability for catalytic activity and durability for structure (Figure S21, Supporting Information).

To further understand the intrinsic mechanism for enhanced HER activity of dual-phased metal carbide electrocatalysts, we try to use ECSA and per-site turnover frequency (TOF) to compare the real performance of catalysts. To obtain the ECSA of catalysts, we measured the electrochemical double layer capacitance ($C_{dl(CFP)}$) of the carbon fiber paper (CFP) substrate (Figure S22, Supporting Information). Assuming a moderate value of 40 μF cm^{-2} for the specific capacitance,[45] after subtracting the $C_{dl(CFP)}$ of CFP, we obtained the ECSA and ECSA-normalized LSV curves (Figure S23, Supporting Information). As can be seen, the dual-phased catalyst has much higher ECSA than the other two single-phased catalysts, which suggests more active sites of the former. More importantly, the MoC-Mo_2C/PNCDs and WC-W_2C/PNCDs both show a high current density of ~0.04 mA cm^{-2} at an overpotential of 200 mV, which is comparable to the reported values.[45] The intrinsic per-site activity of a catalyst is also an important metric for evaluation of catalyst materials.[46] To obtain more insight into the active sites of M_xC/PNCDs, we first measured the LSV curves of the substrate (i.e., CFP) as well as PNCDs loaded on CFP (PNCDs@CFP), the negligible HER activity

from both CFP and PNCDs@CFP relative to carbides suggests the metal carbides are the active components (Figure S24, Supporting Information). To avoid difficulties in distinguishing the activity of different sites, we calculated the TOFs of catalysts, assuming all the metal atoms in the catalysts are active sites (thus the lowest TOF values were calculated), which are determined by inductively coupled plasma atomic emission spectroscopy (ICP-AES).[47] Both dual-phased metal carbide catalysts catalyzed hydrogen evolution in the alkaline electrolyte with a TOF of ~1.3 s^{-1} at an overpotential of 200 mV (Figure S25, Supporting Information). This value is comparable to those exhibited by several non-precious metal HER catalysts, such as NiMo alloy (0.36 s^{-1}),[48] Mo_2C (0.9 s^{-1})[49] and Ni_5P_4 (2.9 s^{-1}).[50] In general, a higher number of exposed active sites contribute to the easy diffusion of the electrolyte during the HER,[12] while higher intrinsic activity of each active site can accelerate the proton mass transport process and shorten the average time for one H_2 molecule to be generated on the electrocatalyst during HER, resulting in the enhancement of electrocatalytic activity.[51] The higher ECSA and TOF of dual-phased carbides jointly suggest that the optimization mechanism of dual-phased carbides could be ascribed to the more exposed active sites and greatly improved catalytic activity of active sites.

Generally, the HER process could be through the Volmer-Heyrovsky or Volmer-Tafel pathways in alkaline media. Unlike in the acidic condition, water dissociation into adsorbed OH^- and H* takes place in the Volmer step, then followed by desorption of OH to refresh the surface and formation of H* for H_2 generation.[52] Due to the strong electrostatic affinity to positively charged Mo/W species and more unfilled d orbitals in MC than M_2C, the generated OH^- would preferentially attach to the MC sites on the MC-M_2C interfaces.[7] While, a pure MC surface is less active for HER due to the weak adsorption energy of H* (0.89 eV for MoC and 0.99 eV for WC) compared with the strong

adsorption energy of H* for Mo_2C (1.07 eV) and W_2C (1.14 eV), which are calculated by density functional theory (DFT) base on the simplified theoretical models (Figure S26,27, Supporting Information). For the pure M_2C surface, the sluggish water dissociation kinetics with higher Tafel slopes results in the deficiency of protons for the subsequent reactions. The adsorbed OH^- species will occupy the active catalytic sites, resulting in a lower ECSA, which is consistent with the measurement results for ECSA of M_2C. The theoretical calculation results match well with the above experimental results, further implying that the increased activity in dual-phase carbides is derived from the combined effect of the exposure of more active sites and the increase in the intrinsic activity of each active site.

In view of the aforementioned considerations, the superior activity of the MC-M_2C/PNCDs is postulated to originate from the following aspects: (i) the highly ordered MO_4 units substituted in the porous ZIF framework increase the dispersion of metal resource within the nitrogen-doped carbon network, resulting in highly dispersed carbide nanocrystals even at high carbonization temperature;[17,43] (ii) the ultrafine carbide nanocrystals confined in porous nitrogen-doped carbon dodecahedrons not only favors the exposure of active sites but also facilitates the charge transport;[10,26] (iii) the abundant nitrogen dopants can function as electron acceptors to assist the carbon atoms in the metal lattice;[16,53] The resulting downshift of the d-band center of metal can enhance the interaction with hydrogen and thus boosts HER performance;[16,54,55] (iv) the strong coupling between MC and M_2C nanocrystals further provides beneficial sites for both water dissociation and hydrogen desorption;[8,11] (v) the geometric confinement of carbides within the PNCDs guarantees the high stability of the electrocatalysts during long-term operation.[56,57]

In summary, we present a facial synthesis of dual-phased carbide nanocrystals consisting of MC

and M_2C (M = Mo or W), which is easily realized through controlling the amount of MO_4 units substituted in the framework of ZIF-8. These ultrafine carbide nanocrystals confined in porous nitrogen-doped carbon dodecahedrons show high catalytic activity and stability as electrocatalysts toward HER in alkaline solution. Moreover, due to the strong coupling interactions between MC and M_2C, the dual-phased MC-M_2C/PNCDs possess favorable modifications of the electronic structures. The resulting moderate adsorption/desorption capability of adsorbed hydrogen intermediates enables dual-phased MC-M_2C/PNCDs much better catalytic activity than single-phased MC/PNCDs and M_2C/PNCDs. This work may provide a new thought to explore efficient electrocatalysts via engineering on composition and nanostructure.

Acknowledgements

X.W.L. acknowledges the funding support from the National Research Foundation (NRF) of Singapore via the NRF Investigatorship (NRF-NRFI2016-04).

References

[1] R. W. Coughlin, M. Farooque, *Nature* **1979**, *279*, 301.

[2] J. Dawson, *Nature* **1974**, *249*, 724.

[3] H. I. Karunadasa, C. J. Chang, J. R. Long, *Nature* **2010**, *464*, 1329.

[4] Z. W. Seh, J. Kibsgaard, C. F. Dickens, I. Chorkendorff, J. K. Norskov, T. F. Jaramillo, *Science* **2017**, *355*.

[5] J. R. Kitchin, J. K. Nørskov, M. A. Barteau, J. G. Chen, *Catal. Today* **2005**, *105*, 66.

[6] W.-F. Chen, J. T. Muckerman, E. Fujita, *Chem. Commun.* **2013**, *49*, 8896.

[7] C. Wan, Y. N. Regmi, B. M. Leonard, *Angew. Chem. Int. Ed.* **2014**, *53*, 6407.

[8] H. Lin, Z. Shi, S. He, X. Yu, S. Wang, Q. Gao, Y. Tang, *Chem. Sci.* **2016**, *7*, 3399.

[9] L. F. Pan, Y. H. Li, S. Yang, P. F. Liu, M. Q. Yu, H. G. Yang, *Chem. Commun.* **2014**, *50*, 13135.

[10] Z. Kou, T. Wang, Y. Cai, C. Guan, Z. Pu, C. Zhu, Y. Hu, A. M. Elshahawy, J. Wang, S. Mu, *Small Methods* **2018**, *2*, 1700396.

[11] P. Xiao, X. Ge, H. Wang, Z. Liu, A. Fisher, X. Wang, *Adv. Funct. Mater.* **2015**, *25*, 1520.

[12] K. Xiong, L. Li, L. Zhang, W. Ding, L. Peng, Y. Wang, S. Chen, S. Tan, Z. Wei, *J. Mater. Chem. A* **2015**, *3*, 1863.

[13] Y. Yan, B. Xia, X. Qi, H. Wang, R. Xu, J. Y. Wang, H. Zhang, X. Wang, *Chem. Commun.* **2013**, *49*, 4884.

[14] F. X. Ma, H. B. Wu, B. Y. Xia, C. Y. Xu, X. W. Lou, *Angew. Chem. Int. Ed.* **2015**, *54*, 15395.

[15] H. Zhang, Z. Ma, G. Liu, L. Shi, J. Tang, H. Pang, K. Wu, T. Takei, J. Zhang, Y. Yamauchi, J. Ye, *NPG Asia Mater.* **2016**, *8*, e293.

[16] Y. Liu, G. Yu, G. D. Li, Y. Sun, T. Asefa, W. Chen, X. Zou, *Angew. Chem. Int. Ed.* **2015**, *54*, 10752.

[17] C. Chen, A. Wu, H. Yan, Y. Xiao, C. Tian, H. Fu, *Chem. Sci.* **2018**, *9*, 4746.

[18] Y. T. Xu, X. Xiao, Z. M. Ye, S. Zhao, R. Shen, C. T. He, J. P. Zhang, Y. Li, X. M. Chen, *J. Am. Chem. Soc.* **2017**, *139*, 5285.

[19] H. Ang, H. T. Tan, Z. M. Luo, Y. Zhang, Y. Y. Guo, G. Guo, H. Zhang, Q. Yan, *Small* **2015**, *11*, 6278.

[20] W. F. Chen, C. H. Wang, K. Sasaki, N. Marinkovic, W. Xu, J. T. Muckerman, Y. Zhu, R. R. Adzic, *Energy Environ. Sci.* **2013**, *6*, 943.

[21] L. Han, M. Xu, Y. Han, Y. Yu, S. Dong, *ChemSusChem* **2016**, *9*, 2784.

[22] L. Zhang, H. Yang, D. K. J. A. Wanigarathna, B. Liu, *Small Methods* **2018**, *2*, 1700353.

[23] L. Huo, B. Liu, Z. Gao, J. Zhang, *J. Mater. Chem. A* **2017**, *5*, 18494.

[24] X. F. Lu, L. F. Gu, J. W. Wang, J. X. Wu, P. Q. Liao, G. R. Li, *Adv. Mater.* **2017**, *29*, 1604437.

[25] H. Zhang, J. Nai, L. Yu, X. W. Lou, *Joule* **2017**, *1*, 77.

[26] H. B. Wu, B. Y. Xia, L. Yu, X. Y. Yu, X. W. Lou, *Nat. Commun.* **2015**, *6*, 6512.

[27] F. Wang, Z. S. Liu, H. Yang, Y. X. Tan, J. Zhang, *Angew. Chem. Int. Ed.* **2011**, *50*, 450.

[28] V. P. Santos, T. A. Wezendonk, J. J. Jaen, A. I. Dugulan, M. A. Nasalevich, H. U. Islam, A. Chojecki, S. Sartipi, X. Sun, A. A. Hakeem, A. C. Koeken, M. Ruitenbeek, T. Davidian, G. R. Meima, G. Sankar, F. Kapteijn, M. Makkee, J. Gascon, *Nat. Commun.* **2015**, *6*, 6451.

[29] C. Avci, J. Ariñez-Soriano, A. Carné-Sánchez, V. Guillerm, C. Carbonell, I. Imaz, D.

Maspoch, *Angew. Chem. Int. Ed.* **2015**, *54*, 14417.

[30] Y. Pan, Y. Liu, G. Zeng, L. Zhao, Z. Lai, *Chem. Commun.* **2011**, *47*, 2071.

[31] Z. Yan, G. He, P. K. Shen, Z. Luo, J. Xie, M. Chen, *J. Mater. Chem. A* **2014**, *2*, 4014.

[32] X. Xu, F. Nosheen, X. Wang, *Chem. Mater.* **2016**, *28*, 6313.

[33] Z. Yang, T. Zhao, X. Huang, X. Chu, T. Tang, Y. Ju, Q. Wang, Y. Hou, S. Gao, *Chem. Sci.* **2017**, *8*, 473.

[34] A. Meffre, B. Mehdaoui, V. Kelsen, P. F. Fazzini, J. Carrey, S. Lachaize, M. Respaud, B. Chaudret, *Nano Lett.* **2012**, *12*, 4722.

[35] J. Greeley, T. F. Jaramillo, J. Bonde, I. B. Chorkendorff, J. K. Norskov, *Nat. Mater.* **2006**, *5*, 909.

[36] R. Michalsky, Y.-J. Zhang, A. A. Peterson, *ACS Catal.* **2014**, *4*, 1274.

[37] V. Heine, *Phys. Rev.* **1967**, *153*, 673.

[38] L. Ramqvist, *J. Appl. Phys.* **1971**, *42*, 2113.

[39] C. He, J. Tao, *Chem. Commun.* **2015**, *51*, 8323.

[40] C. Lv, Z. Huang, Q. Yang, C. Zhang, *Energy Technol.* **2018**, *6*, 1707.

[41] X. Geng, W. Sun, W. Wu, B. Chen, A. Al-Hilo, M. Benamara, H. Zhu, F. Watanabe, J. Cui, T. P. Chen, *Nat. Commun.* **2016**, *7*, 10672.

[42] P. Xiao, M. A. Sk, L. Thia, X. Ge, R. J. Lim, J.-Y. Wang, K. H. Lim, X. Wang, *Energy Environ. Sci.* **2014**, *7*, 2624.

[43] Z.-Y. Wu, B.-C. Hu, P. Wu, H.-W. Liang, Z.-L. Yu, Y. Lin, Y.-R. Zheng, Z. Li, S.-H. Yu, *NPG Asia Mater.* **2016**, *8*, e288.

[44] Y. Y. Chen, Y. Zhang, W. J. Jiang, X. Zhang, Z. Dai, L. J. Wan, J. S. Hu, *ACS Nano* **2016**, *10*, 8851.

[45] C. C. McCrory, S. Jung, I. M. Ferrer, S. M. Chatman, J. C. Peters, T. F. Jaramillo, *J. Am. Chem. Soc.* **2015**, *137*, 4347.

[46] J. D. Benck, T. R. Hellstern, J. Kibsgaard, P. Chakthranont, T. F. Jaramillo, *ACS Catal.* **2014**, *4*, 3957.

[47] J. Wang, W. Chen, T. Wang, N. Bate, C. Wang, E. Wang, *Nano Res.* **2018**, *11*, 4535.

[48] J. R. McKone, B. F. Sadtler, C. A. Werlang, N. S. Lewis, H. B. Gray, *ACS Catal.* **2013**, *3*, 166.

[49] L. Ma, L. R. L. Ting, V. Molinari, C. Giordano, B. S. Yeo, *J. Mater. Chem. A* **2015**, *3*, 8361.

[50] A. B. Laursen, K. R. Patraju, M. J. Whitaker, M. Retuerto, T. Sarkar, N. Yao, K. V. Ramanujachary, M. Greenblatt, G. C. Dismukes, *Energy Environ. Sci.* **2015**, *8*, 1027.

[51] H. Ang, H. Wang, B. Li, Y. Zong, X. Wang, Q. Yan, *Small* **2016**, *12*, 2859.

[52] M. Gong, W. Zhou, M.-C. Tsai, J. Zhou, M. Guan, M.-C. Lin, B. Zhang, Y. Hu, D.-Y. Wang, J. Yang, *Nat. Commun.* **2014**, *5*, 4695.

[53] Y. Zheng, *ACS Nano* **2014**, *8*, 5290.

[54] R. Levy, M. Boudart, *Science* **1973**, *181*, 547.

[55] S. Oyama, *Catal. Today* **1992**, *15*, 179.

[56] H. Zhang, Z. Ma, J. Duan, H. Liu, G. Liu, T. Wang, K. Chang, M. Li, L. Shi, X. Meng, *ACS Nano* **2015**, *10*, 684.

[57] X. Zou, X. Huang, A. Goswami, R. Silva, B. R. Sathe, E. Mikmeková, T. Asefa, *Angew. Chem. Int. Ed.* **2014**, *53*, 4372.

Figures and captions

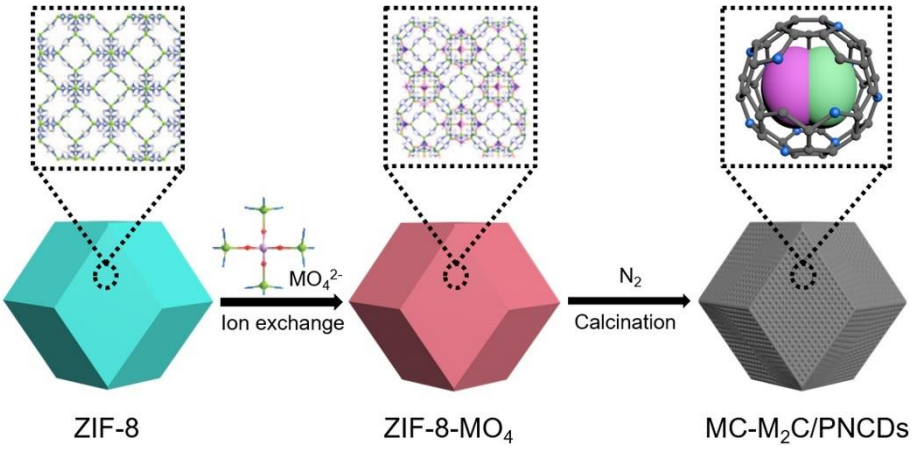

Figure 1. Schematic illustration of the MC-M_2C/PNCDs.

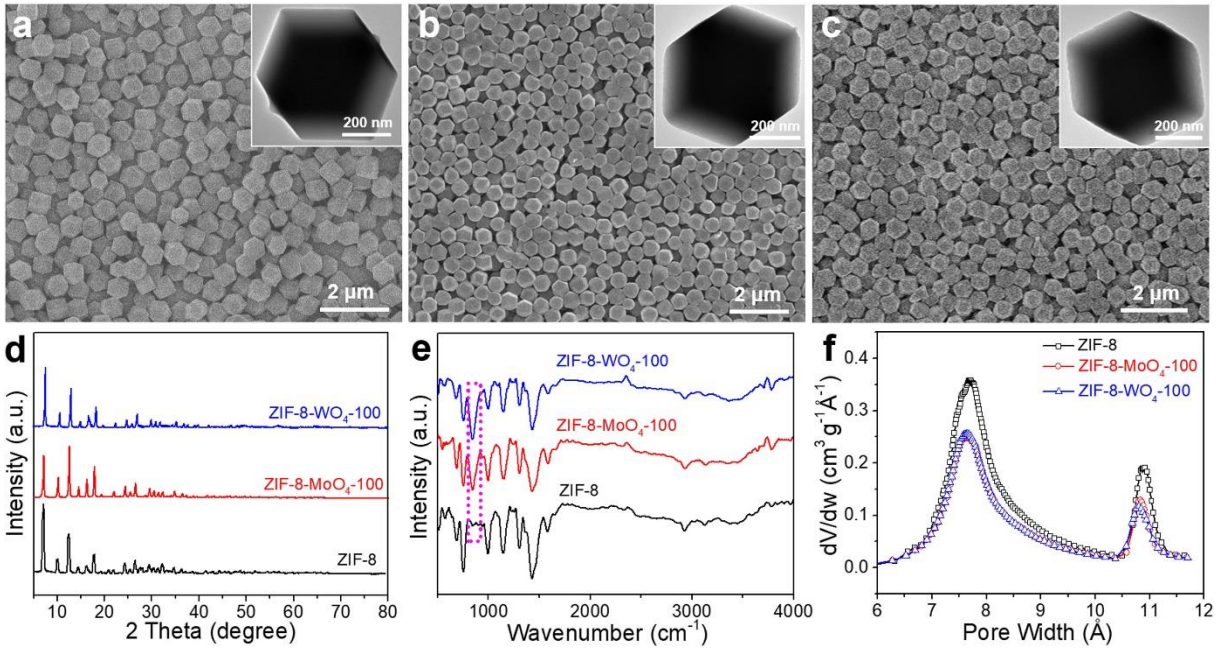

Figure 2. FESEM images of (a) ZIF-8, (b) ZIF-8-MoO_4-100 and (c) ZIF-8-WO_4-100 (Insets: TEM images). (d) XRD patterns, (e) FTIR spectra and (f) the pore size distribution of the as-prepared ZIF-8, ZIF-8-MoO_4-100 and ZIF-8-WO_4-100.

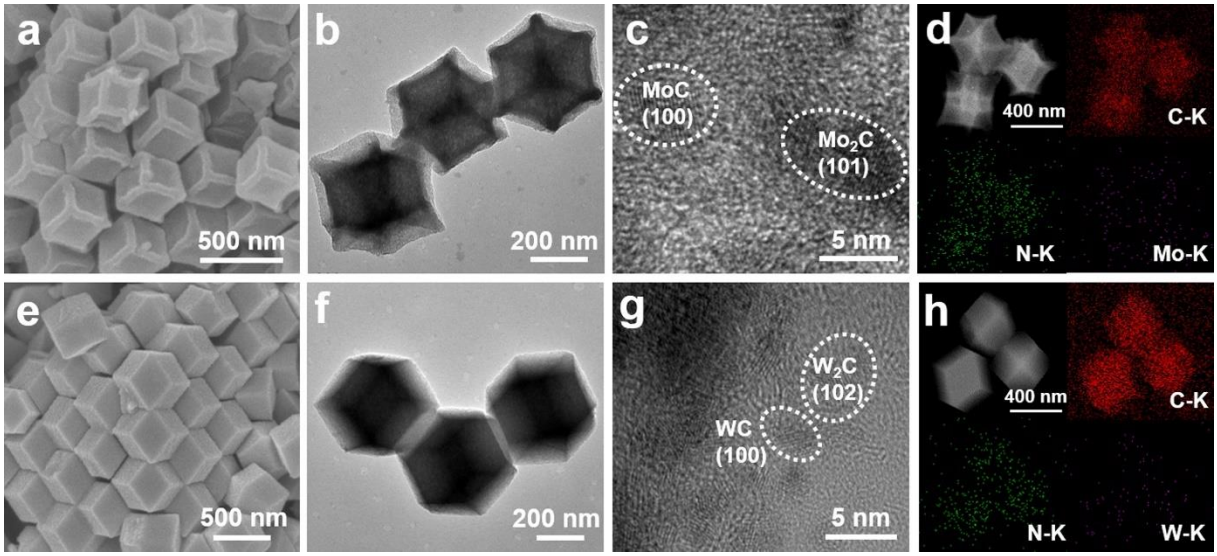

Figure 3. (a) FESEM, (b) TEM, (c) HRTEM images and (d) elemental mapping of MoC-Mo_2C/PNCDs. (e) FESEM, (f) TEM, (g) HRTEM images and (h) elemental mapping of WC-W_2C/PNCDs.

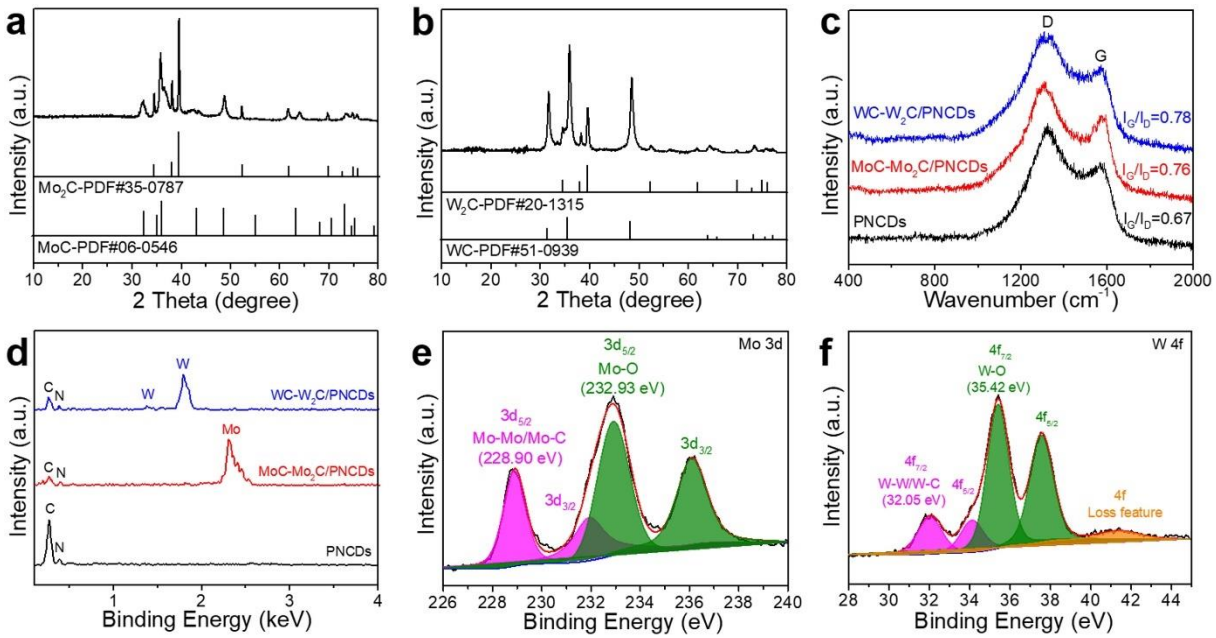

Figure 4. XRD patterns of (a) MoC-Mo_2C/PNCDs and (b) WC-W_2C/PNCDs. (c) Raman and (d) EDX spectra of PNCDs, MoC-Mo_2C/PNCDs and WC-W_2C/PNCDs. High-resolution XPS spectra of (e) Mo 3d for MoC-Mo_2C/PNCDs, and (f) W 4f for WC-W_2C/PNCDs.

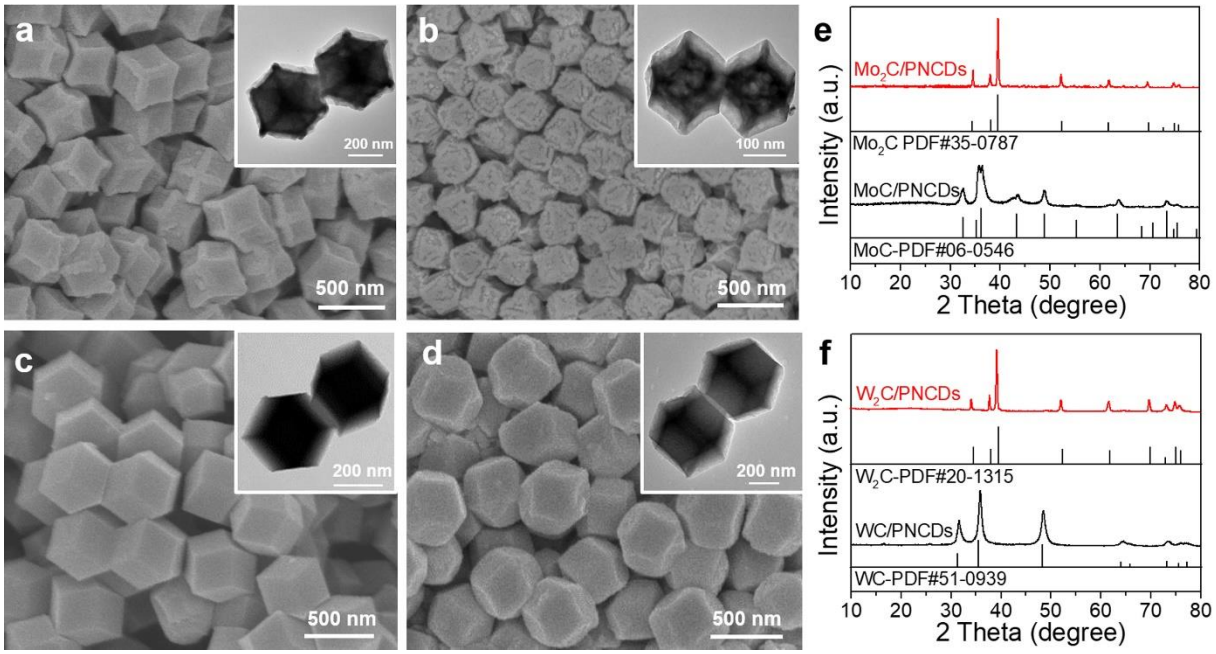

Figure 5. FESEM and TEM (Insets) images of (a) MoC/PNCDs, (b) Mo_2C/PNCDs, (c) WC/PNCDs and (d) W_2C/PNCDs. XRD patterns of (e) MoC/PNCDs and Mo_2C/PNCDs; (f) WC/PNCDs and W_2C/PNCDs.

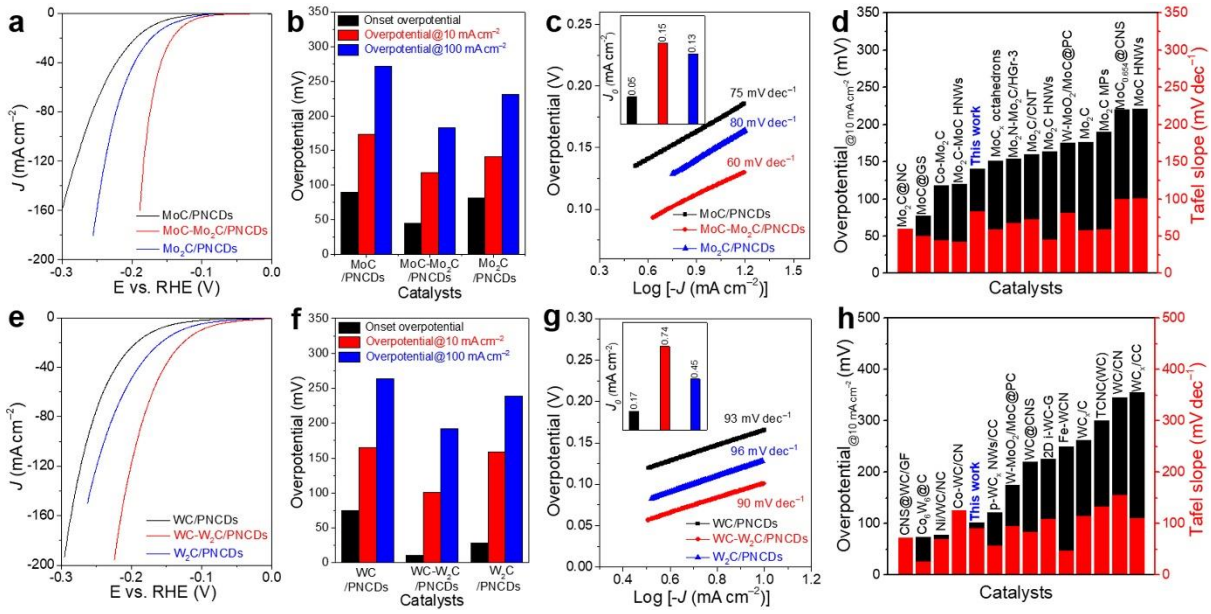

Figure 6. LSV curves of (a) Mo$_x$C/PNCDs and (e) W$_x$C/PNCDs. Comparison of onset overpotential and overpotentials at 10 and 100 mA cm^{-2} of (b) MoC/PNCDs, MoC-Mo$_2$C/PNCDs, Mo$_2$C/PNCDs; and (f) WC/PNCDs, WC-W$_2$C/PNCDs, W$_2$C/PNCDs. Tafel slopes of (c) MoC/PNCDs, MoC-Mo$_2$C/PNCDs, Mo$_2$C/PNCDs; and (g) WC/PNCDs, WC-W$_2$C/PNCDs, W$_2$C/PNCDs (Insets: Histograms of exchange current density). HER activity comparison graph showing overpotentials at a current density of 10 mA cm^{-2} and Tafel slopes measured in an alkaline solution for (d) molybdenum carbide-based, and (h) tungsten carbide-based catalysts reported in the recent years.

for Table of Content Entry

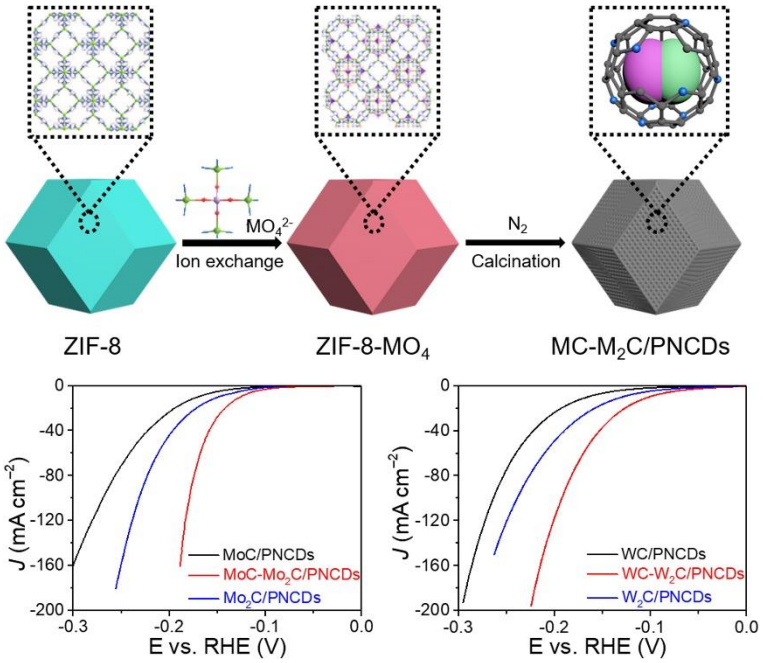

Dual-phased carbide nanocrystals consisting of MC and M_2C (M = Mo or W) are realized through controlling the amount of MO_4 units substituted in the framework of ZIF-8. Owing to the desired composition and ultrafine structures, the dual-phased MC-M_2C/PNCDs exhibit better catalytic performances towards hydrogen evolution reaction than single-phased MC/PNCDs and M_2C/PNCDs.